ChemComm

COMMUNICATION

View Article Online
View Journal | View Issue

Cite this: *Chem. Commun.*, 2018, **54**, 8717

Received 30th June 2018,
Accepted 9th July 2018

DOI: 10.1039/c8cc05259j

rsc.li/chemcomm

Novel D–A–D based near-infrared probes for the detection of β-amyloid and Tau fibrils in Alzheimer's disease†

Yuying Li,[a] Kan Wang,[b] Kaixiang Zhou,[a] Wentao Guo,[a] Bin Dai,[b] Yi Liang,*[b] Jiapei Dai[c] and Mengchao Cui*[a]

Novel D–π–A–π–D probes were investigated for the detection of Aβ plaques and NFTs. The probes displayed remarkable optical properties, and DADNIR-2 possessed high affinity towards Tau and Aβ aggregates (K_d = 0.41 nM and 1.04 nM, respectively) with certain selectivity. DADNIR-2 could penetrate the BBB and label Aβ plaques *in vivo*.

Alzheimer's disease (AD) is a progressive neurodegenerative disease, which causes cognitive deficits that worsen over years.[1,2] Extracellular β-amyloid (Aβ) plaques and intraneuronal neurofibrillary tangles (NFTs) have been both wildly accepted as important pathological hallmarks of AD.[3,4] According to an amyloid cascade hypothesis, Aβ is an important biomarker for the early diagnosis of AD and anti-Aβ drug development because it appeared in the initial stage and gradually caused the death of neurons.[5–7] Intraneuronal NFTs as another biomarker, which is composed of abnormal hyperphosphorylated Tau aggregates in neurons, were found to have a more significant correlation with the degree of cognitive impairment than Aβ.[3,8,9] Thus, these two biomarkers have drawn extensive attention recently.[10–12]

Exquisite sensitivity, high resolution, real time imaging and low-cost near-infrared fluorescence (NIRF) imaging has been a remarkable technology in recent years, which allows deep penetration and avoids auto-fluorescence from bio-tissues.[13,14] However, due to the strong shielding effect of human cranium, NIR light is hardly detectable, but for small animals, NIRF imaging is a rapid, simple and effective tool for diagnosis and drug screening in animal models. At the molecular level, the spatial configuration of Aβ and Tau proteins shared a common misfolded cross-β structure to form a hydrophobic cavum, which played a pivotal role in small ligand recognition.[15,16] A hydrophobic groove formed between Val18 and Phe20 was the prime site when probes interacted with Aβ fibrils, and the probes have a propensity to enter the groove along the fibril axis.[17] Thus, flat and slim molecules tended to display high affinity to Aβ. The reported NIR probes, as exemplified by **CRANAD-2**,[18] **DANIR 2c**,[19] **DANIR 3b**,[20] **BAP-1**[21] and **YHY2**,[22] possess favorable affinity to Aβ fibrils benefitted from their specific structures. In the Tau filaments, the core combined two identical proto-filaments through a cross-β/β-helix structure, which define the parallel β-sheet structure of aggregation.[15] In this context, recent studies proposed that it is beneficial for NFT selectivity when the core length of the probes is 13 to 19 Å.[23] Derived from the existing Aβ probes, most of the reported Tau probes were designed with longer backbone length, including extended benzothiazole analogs **PBBs**[23] and boron dipyrromethane derivatives **TAU 1** and **TAU 2**.[24]

At present, most of the NIR probes were based on the D–π–A or D–π–A–π–D structure, architected by an electron rich donor (D) and an electron deficient acceptor (A) and bridged by a conjugated π system. This structure displays an excellent rigid planarity and capability of electronic transmission, beneficially pushing the emission wavelength into the NIR region. In consideration of the backbone length and planarity, novel probes with a D–π–A–π–D structure were designed, synthesized and evaluated. These probes were supposed to meet favorable core length for the selectivity of NFTs while possessed excellent rigid planar structures to benefit for optical properties and interaction with the β-sheet structure. According to previous studies, the *N*,*N*-dimethylamino group is an ideal electron-donor, and plays an important role in recognizing the β-sheet structure. Meanwhile, the low molecular weight and planar configuration of the dicyano acceptor possessed penetrable blood–brain barrier (BBB). Previous reports demonstrated that the improvement of optical properties and the optimization of the

[a] *Key Laboratory of Radiopharmaceuticals, Ministry of Education, College of Chemistry, Beijing Normal University, Beijing 100875, China. E-mail: cmc@bnu.edu.cn*
[b] *State Key Laboratory of Virology, College of Life Sciences, Wuhan University, Wuhan 430072, China. E-mail: liangyi@whu.edu.cn*
[c] *Wuhan Institute for Neuroscience and Neuroengineering, South-Central University for Nationalities, Wuhan 430074, China*

† Electronic supplementary information (ESI) available: Experimental details, absorption and fluorecence spectra, saturation binding curves, *in vitro* fluorescence images, and ^{1}H-NMR, ^{13}C-NMR and HRMS spectra. See DOI: 10.1039/c8cc05259j

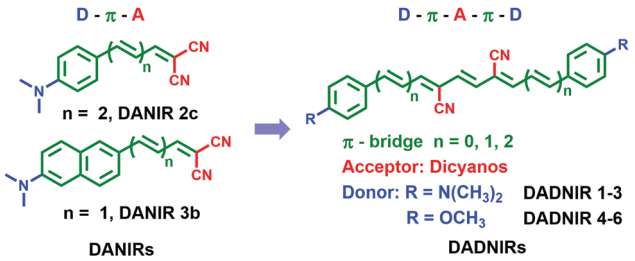

Scheme 1 Design of the novel D–π–A–π–D probes.

binding ability could be achieved by lengthening the polyenic chains,[19,20,25] and it is an efficient method to extend the backbone length. Herein, the probes with a *N*,*N*-dimethylamino donor, a cyano acceptor and different lengths of polyenic chains as π-bridges were employed. Besides, a set of compounds with a methoxy group as the electron-donor moiety were also designed and evaluated to explore the influence of different functional groups.

The final probes (**DADNIR 1–6**), illustrated in Scheme 1, were successfully obtained *via* typical Knoevenagel condensation from 3-hexenedinitrile and *para* substituted aldehydes, using minor modified procedures from the literature.[26] After the reaction, due to poor solubility, the pure products could be easily separated from the reaction solution by filtration or recrystallization in acceptable yields. The *para* substituted aldehydes **3** and **6** with an extended *trans* carbon–carbon double bond were prepared through the Witting reaction from commercially available *trans*-cinnamaldehydes in yields of 39% and 32%, respectively.[27]

The major sensing mechanism of the D–π–A–π–D structures could be explained by intramolecular charge transfer (ICT).[28,29] Benefitted from the conjugated rigid planar structure and conducive electronic attraction of the cyano group, **DADNIRs** possessed a favorable capability of undergoing electronic transmission. The prominent red shift of wavelengths (Table S1, ESI†) was observed with an expanded π-bridge, and pushed these probes into the NIR region in PBS. It should be noticed the emission maxima of **DADNIR-1** with a shorter π-bridge between the donor and the acceptor (λ_{em} = 650 nm), basically equated with **DANIR 2c** (λ_{em} = 665 nm) and **DANIR 3b** (λ_{em} = 682 nm) in PBS, which verified that the D–π–A–π–D scaffold is better than the D–π–A structure to push the probes into the NIR region. However, compared with **DADNIR 1–3**, **DADNIR 4–6** displayed a significant reduction of emission maxima, indicating that the electron-donating ability of the methoxy group is much weaker than that of the *N*,*N*-dimethylamino group. In addition, large Stokes shifts (70–200 nm) were observed, which were beneficial for bio-imaging. To address the photo-stability of **DADNIR-2** against bleaching, we measured the photodegradation of **DADNIR-2** with constant illumination over 30 min, as shown in the Fig. S4 (ESI†), **DADNIR-2** displayed weak photobleaching in this experiment.

Then we tested these **DADNIRs** upon interaction with an aggregated recombinant Tau fragment (k18), $A\beta_{1-42}$ aggregates and bovine serum albumin (BSA, as a model of non-specific binding in blood). As shown in Table 1, except for **DADNIR-3** and **DADNIR-6** with total seven conjugated double bonds (n = 2), other probes displayed significant fluorescence enhancement with $A\beta_{1-42}$ aggregates (19–93 fold). As for the interaction with Tau aggregates, **DADNIR-2**, **DADNIR-4** and **DADNIR-5** exhibited obvious fluorescence enhancement, especially **DADNIR-2** possessed a strong increase (48-fold) (Fig. 1A and B and Table 1). Besides, a considerable hypsochromic shift of emission maxima was observed upon interaction with the Aβ and Tau aggregates in PBS (33–104 nm), and there is not much difference between Tau and Aβ. These phenomena indicate that **DADNIRs** entered the hydrophobic 16-KLVFFA-21 channel of the Aβ aggregates and the 306-VQIVYK-311 channel of the Tau aggregates, causing the destabilization of micro environmental polarity, and this is in accord with the significant solvent dependency of ICT molecules.[30] Meanwhile, hydrophobic interaction is considered to be the driving force for binding to the Aβ and Tau aggregates, the two phenyl rings in **DADNIRs** may form π–π stacking with the repeated aromatic residues in the hydrophobic channel, and the dicyano groups in the middle of **DADNIRs** may form hydrogen bonding interaction with the tyrosine residues in the Tau aggregates. For direct comparison, we measured the fluorescence enhancement of the reported Aβ specific probe **BAP-1** and Tau specific probes **TAU 1** and **TAU 2** under identical conditions. The fluorescence enhancements of **BAP-1** (65-fold) with $A\beta_{1-42}$ aggregates, **TAU 1** (9.4-fold) and **TAU 2** (4.5-fold) with the Tau

Table 1 The calculated partition coefficient ($c\log P$), core length, emission maxima (λ_{em}), saturation binding constants (K_d), and the maximum fluorescence fold increase of **DADNIRs**, **TAU 1**, **TAU 2** and **BAP-1**

				λ_{em}[d] (nm)		Fold		K_d[e] (nM)	
Probes	$c\log P$[a]	Length[b] (Å)	λ_{em}[c] (nm)	Aβ	Tau	Aβ	Tau	Aβ	Tau
DADNIR-1	5.04	13.39	650	546	546	93	2	16.89 ± 0.47	n.d.
DADNIR-2	5.92	17.91	690	642	651	70	48	1.04 ± 0.03	0.41 ± 0.20
DADNIR-3	6.67	22.47	828	650	650	1	1	n.d.	n.d.
DADNIR-4	4.25	13.39	540	470	465	82	2	1.13 ± 0.03	n.d.
DADNIR-5	5.55	17.91	610	577	550	19	17	116.56 ± 7.14	153.20 ± 18.09
DADNIR-6	6.64	22.47	668	600	600	1	1	n.d.	n.d.
TAU 1	3.73	13.9[f]	705[f,g]	733	775	16	9, 6.4[f]	2.86 ± 0.54	324.93 ± 75.24
TAU 2	4.32	13.8[f]	687[f,g]	679	720	83	5, 9.3[f]	1.19 ± 0.23	161.10 ± 41.72
BAP-1	3.24	11.4[f]	648[f,g]	675	675	65	9	30.26 ± 3.37 44.1[f]	189.25 ± 31.87

[a] Calculated using the online ALOGPS 2.1 program. [b] Calculated using the SYBYL-X 2.0 program. [c] Emission maxima measured in PBS (10% ethanol). [d] Emission maxima measured by interaction with protein aggregates in PBS (10% ethanol). [e] Measured in triplicate with results given as the mean ± SD. [f] Reference value. [g] Measured in $CHCl_3$. n.d., not determined.

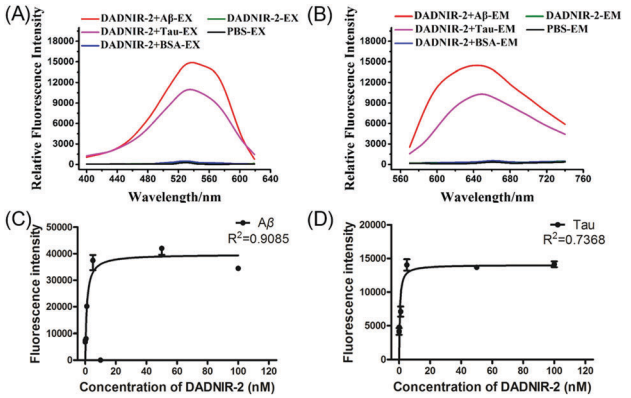

Fig. 1 Excitation spectra (A) and emission spectra (B) of **DADNIR-2** (50 nM) in the presence of proteins (10 μg mL^{-1}). Saturation binding curve of **DADNIR-2** with $A\beta_{1-42}$ aggregates (C) and Tau (k18) aggregates (D).

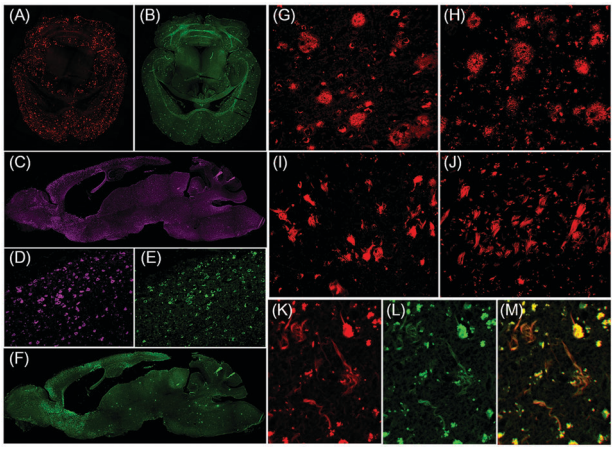

Fig. 2 *In vitro* fluorescence images of **DADNIR-2**. (A) Tg mice (C57BL6, APPsw/PSEN1, 22 month old, male), 5×. (C) Tg mice (C57BL6, rTg4510, 7 month old, female), 4×. Counter staining using ThS (B, 5×) and AT8 (F, 4×). The details of Tg mice stained by AT8 (E, 20×) and **DADNIR-2** (D, 20×). (G) AD patient (temporal lobe, 64 year-old, female), 20×. (H) AD patient (temporal lobe, 91 year-old, male), 20×. (I) AD patient (entorhinal cortex, 85 year-old, male), 20×. (J) AD patient (hippocampus, 95 year-old, female), 20×. Immunofluorescence imaging of **DADNIR-2** (K, 20×) and AT8 (L, 20×) on the brain section of AD patients. (M) Merged image of K and L, 20×. RFP and a Txred filter was used for **DADNIR-2**, and a GFP filter for ThS and AT8.

aggregates were consistent with the reported values. However, a significant fluorescence enhancement was observed for **TAU 1** (16-fold) and **TAU 2** (83-fold) upon interaction with $A\beta_{1-42}$ aggregates, which indicated that these probes also bind to Aβ fibrils.

Next, *in vitro* fluorescence saturation binding assay was conducted to estimate the binding affinities of the probes to the Aβ and Tau aggregates quantitatively (Table 1). **BAP-1**, **TAU 1** and **TAU 2** were also measured under the same assay conditions for comparison. The K_d value of **BAP-1** for $A\beta_{1-42}$ was measured to be 30.26 nM (Table 1), which is consistent with the reported value. While **TAU 1** and **TAU 2**, analogues of **BAP-1**, displayed moderate affinities towards the Tau aggregates with K_d values of 324.93 nM and 161.10 nM, respectively. However, in agreement with the fluorescence enhancement results, **TAU 1** and **TAU 2** displayed remarkable binding affinity to the $A\beta_{1-42}$ aggregates with K_d values of 2.86 nM and 1.19 nM, respectively, even more significant than **BAP-1**. In accord with the fluorescence enhancement results, **DADNIR-2** exhibited high affinities to $A\beta_{1-42}$ fibrils (Fig. 1C) and Tau aggregates (Fig. 1D), with K_d values of 1.04 nM and 0.41 nM, and showed certain selectivity (2.54) towards Tau over Aβ. However, **DADNIR-5** with the same core length but a methoxy electron donor, displayed decreased binding affinity for both aggregates (116.56 nM and 153.20 nM for Aβ and Tau proteins, respectively). In addition, **DADNIR-1** (K_d = 16.89 nM) and **DADNIR-4** (K_d = 1.13 nM) displayed high affinity to $A\beta_{1-42}$ aggregates while no apparent interaction with the Tau protein. These results indeed support the viewpoint that shorter distance is beneficial for Aβ binding, and the selectivity (Tau over Aβ) could be achieved by extending the molecular length. However, the core length should be distributed in a suitable range (15–19 Å), which can explain that **DADNIR-3** and **DADNIR-6** (22.47 Å) displayed very few interactions with the Tau aggregates.

In vitro neuropathological staining was conducted in brain tissues to evaluate the binding ability and selectivity of these probes. Numerous fluorescence spots were labeled by **DADNIR-2** on the brain section from transgenic (Tg) mice (C57BL6, APPsw/PSEN1, AD model with Aβ deposition) (Fig. 2A), while no specific labeling was found on wild-type (WT) control mice (C57BL6) (Fig. S12A, ESI†). These glaring spots were confirmed to be Aβ plaques by Thioflavin S (ThS) staining (Fig. 2B). Compared with ThS, **DADNIR-2** displayed a much higher signal-to-noise ratio with an almost invisible background. In addition, the circular fluorescent plaques in Fig. 2G and H illustrated that **DADNIR-2** can clearly stain the Aβ plaques of AD patients. As expected, many bright spots of Tg mice (C57BL6, rTg4510, Tau model) (Fig. 2C) were observed, and confirmed by immunofluorescence staining (Fig. 2F). In Fig. 2I and J, flame like structures with a well-defined border revealed that **DADNIR-2** distinctly stained the NFTs on the brain section of AD patients. The merged image (Fig. 2M, in yellow) of immunofluorescence showed the co-localization of **DADNIR-2** and a p-tau antibody (AT8), which demonstrated that the NFTs were specifically labeled by **DADNIR-2**. **DADNIR-1** (Fig. S13, ESI†), **DADNIR-4** (Fig. S15, ESI†) and **DADNIR-5** (Fig. S16, ESI†) displayed weak staining of Aβ plaques on the AD patients' brain sections, and the contrast was unsatisfactory. In addition, **DADNIR-3** (Fig. S14, ESI†) and **DADNIR-6** (Fig. S17, ESI†) displayed negative results on the staining sections. In accord with the binding results, **BAP-1**, **TAU 1** and **TAU 2** clearly displayed very positive Aβ plaques staining on the AD brain sections (Fig. S18, ESI†).

The cytotoxicity study of **DADNIR-2** was performed by MTT assay using a human neuronal cell line (SH-SY5Y) at different concentrations. Meanwhile, the phototoxicity test was finished under the same conditions. As shown in Fig. S19 (ESI†), **DADNIR-2** showed no marked toxicity to the neuronal cell line at 1 μM. To evaluate the ability to penetrate the BBB of **DADNIR-2**, we tested this parameter using the HPLC based method on normal ICR mice.[27] The brain samples were treated by the procedures reported previously, and were analyzed by HPLC.

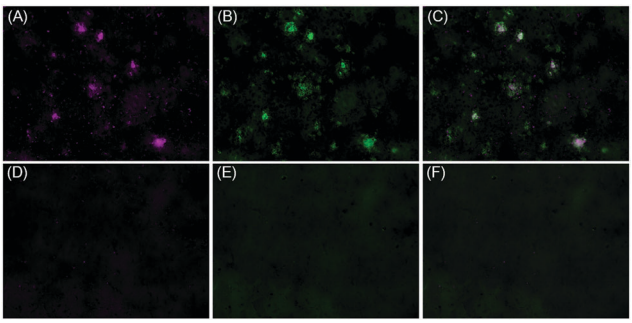

Fig. 3 *Ex vivo* fluorescence images of (A) Tg mouse (C57BL6, APPsw/PSEN1, 24-month old, male), and (D) WT mouse (C57BL6, 24-month old, male) of **DADNIR-2** using a TexasRed filter, 10×. (B and E) Counterstained by ThS using a GFP filter, 10×. (C and F) The merged images showing the co-localization of **DADNIR-2** and ThS, 10×.

The BBB penetrability for **DADNIR-2** at 2 min was calculated to be 2.14 ± 0.12% ID per g, which is in a moderate level, and the HPLC profile demonstrated that **DADNIR-2** was biologically stable in the brain. In addition, the *ex vivo* biodistribution was implemented in ICR mice of different time points. As shown in Fig. S20 (ESI†), the probes possessed a moderate BBB penetrability and cleared quickly from the brain in normal mice. However, the scalp had a strong auto-fluorescence, and the fluorescence of the brain was shielded. In addition, **DADNIR-2** was mainly accumulated in the liver and metabolized through the kidneys (Fig. S20C, ESI†).

In order to further verify the potential use of **DADNIR-2** *in vivo*, *ex vivo* fluorescence staining was performed on a Tg mouse and an age-matched WT mouse. As shown in Fig. 3A, **DADNIR-2** specifically labeled Aβ plaques in the brain of the Tg mouse. Compared with the control mouse (Fig. 3D), there were many bright spots on the sections of the Tg mouse, and the stained Aβ plaques were confirmed by ThS (Fig. 3B). The merged image (Fig. 3C) showed the co-localization of **DADNIR-2** and ThS in white patches. The *ex vivo* fluorescence staining demonstrated that **DADNIR-2** penetrates the BBB and is specifically bound to Aβ plaques in the brain.

In summary, two sets of fluorescent probes with a D–π–A–π–D structure were designed, synthesized and evaluated as NIRF imaging probes for the detection of AD biomarkers. The emission maxima of these probes were dominated by the length of a conjugated π system and the electron donating ability of substituents. And the selectivity for NFTs could be achieved by controlling the backbone length of the probes. Among these probes, **DADNIR-2** displayed high binding affinity toward Tau and Aβ aggregates as well as certain selectivity for Tau proteins. As expected, **DADNIR-2** clearly stained NFTs on the brain sections of Tg mice and AD patients, and the result was verified by immunofluorescence counterstaining. Besides, Aβ plaques in AD patients and Tg mice were also efficiently stained by **DADNIR-2**, and displayed a high signal-to-noise ratio. In addition, **DADNIR-2** possessed favorable photostability and phototoxicity. Finally, the BBB penetrability of **DADNIR-2** in normal mice was at a moderate level of 2.14% ID per g, meanwhile the specific labeling of Aβ plaques was also confirmed by *ex vivo* fluorescence staining. Thus **DADNIR-2** may serve as a potential NIRF probe for the detection of biomarkers in AD.

This work was funded by the National Natural Science Foundation of China (No. 21571022, 31570779, and 31770833), the Beijing Municipal Natural Science Foundation (No. 7182089), and the Fundamental Research Fund for the Central Universities of China (No. 2015204020201). The authors thank Dr Jin Liu (College of Life Science, Beijing Normal University) for the assistance in the *in vitro* neuropathological staining.

Conflicts of interest

There are no conflicts to declare.

Notes and references

1 H. Braak and E. Braak, *Acta Neuropathol.*, 1991, **82**, 239–259.
2 E. Karran, M. Mercken and B. S. De, *Nat. Rev. Drug Discovery*, 2011, **10**, 698–712.
3 K. Iqbal, A. C. Alonso, S. Chen, M. O. Chohan, E. Elakkad, C. X. Gong, S. Khatoon, B. Li, F. Liu and A. Rahman, *Biochim. Biophys. Acta*, 2005, **1739**, 198–210.
4 V. L. Villemagne, *J. Nucl. Med.*, 2017, **59**, 175–176.
5 J. A. Hardy and G. A. Higgins, *Science*, 1992, **256**, 184–185.
6 L. Mucke, *Nature*, 2009, **461**, 895–897.
7 J. Hardy and D. J. Selkoe, *Science*, 2002, **297**, 353–356.
8 J. Avila, *FEBS Lett.*, 2006, **580**, 2922–2927.
9 J. L. Price, D. W. Mckeel, V. D. Buckles, C. M. Roe, C. Xiong, M. Grundman, L. A. Hansen, R. C. Petersen, J. E. Parisi and D. W. Dickson, *Neurobiol. Aging*, 2009, **30**, 1026–1036.
10 H. Fu and M. Cui, *Curr. Med. Chem.*, 2018, **25**, 2736–2759.
11 W. Dou, W. Chen, X. He, J. Su and H. Tian, *Faraday Discuss.*, 2016, **196**, 395–402.
12 W. Zhang, J. Arteaga, D. K. Cashion, G. Chen, U. Gangadharmath, L. F. Gomez, D. Kasi, C. Lam, Q. Liang and C. Liu, *J. Alzheimer's Dis.*, 2012, **31**, 601–612.
13 R. Weissleder, *Nat. Biotechnol.*, 2001, **19**, 316–317.
14 H. Tong, K. Lou and W. Wang, *Acta Pharm. Sin. B*, 2015, **5**, 25–33.
15 A. W. P. Fitzpatrick, B. Falcon, S. He, A. G. Murzin, G. Murshudov, H. J. Garringer, R. A. Crowther, B. Ghetti, M. Goedert and S. H. W. Scheres, *Nature*, 2017, **547**, 185–190.
16 L. Gremer, D. Schölzel, C. Schenk, E. Reinartz, J. Labahn, R. Ravelli, M. Tusche, C. LopezIglesias, W. Hoyer and H. Heise, *Science*, 2017, **358**, 116–119.
17 C. Wu, Z. Wang, H. Lei, W. Zhang and Y. Duan, *J. Am. Chem. Soc.*, 2007, **129**, 1225–1232.
18 C. Ran, X. Xu, S. B. Raymond, B. J. Ferrara, K. Neal, B. J. Bacskai, Z. Medarova and A. Moore, *J. Am. Chem. Soc.*, 2009, **131**, 15257–15261.
19 M. Cui, M. Ono, H. Watanabe, H. Kimura, B. Liu and H. Saji, *J. Am. Chem. Soc.*, 2014, **136**, 3388–3394.
20 H. Fu, M. Cui, L. Zhao, P. Tu, K. Zhou, J. Dai and B. Liu, *J. Med. Chem.*, 2015, **58**, 6972–6983.
21 M. Ono, H. Watanabe, H. Kimura and H. Saji, *ACS Chem. Neurosci.*, 2012, **3**, 319–324.
22 H. Yang, J. Zhang, Y. Zang, H. Zhang, J. Li, G. Chen and X. He, *Dyes Pigm.*, 2017, **136**, 224–228.
23 M. Maruyama, H. Shimada, T. Suhara, H. Shinotoh, B. Ji, J. Maeda, M. R. Zhang, J. Trojanowski, V. Y. Lee and M. Ono, *Neuron*, 2013, **79**, 1094–1108.
24 P. Verwilst, H. R. Kim, J. Seo, N. W. Sohn, S. Y. Cha, Y. Kim, S. Maeng, J. W. Shin, J. H. Kwak and C. Kang, *J. Am. Chem. Soc.*, 2017, **139**, 13393–13403.
25 K. Zhou, H. Bai, L. Feng, J. Dai and M. Cui, *Anal. Chem.*, 2017, **89**, 9432–9437.
26 J. S. Meisner, D. F. Sedbrook, M. Krikorian, J. Chen, A. Sattler, M. E. Carnes, C. B. Murray, M. Steigerwald and C. Nuckolls, *Chem. Sci.*, 2012, **3**, 1007–1014.
27 K. Zhou, H. Fu, L. Feng, M. Cui, J. Dai and B. Liu, *Chem. Commun.*, 2015, **51**, 11665–11668.
28 T. Yoshihara, S. I. Druzhinin and K. A. Zachariasse, *J. Am. Chem. Soc.*, 2004, **126**, 8535–8539.
29 S. Sasaki, G. Drummen and G. I. Konishi, *J. Mater. Chem.*, 2016, **4**, 2731–2743.
30 J. R. Lakowicz, Principles of Fluorescence Spectroscopy, *Solvent and Environmental Effects*, Springer US, Boston, MA, 2006, pp. 205–235.

